Progressive remote memory decline coincides with parvalbumin interneuron hyperexcitability and enhanced inhibition of cortical engram cells in a mouse model of Alzheimer's disease

Julia J. van Adrichem[1], Rolinka J. van der Loo[1], August B. Smit[1], Michel C. van den Oever[1, *], Ronald E. van Kesteren[1, *]

[1]Department of Molecular and Cellular Neurobiology, Center for Neurogenomics and Cognitive Research, Amsterdam Neuroscience, Vrije Universiteit Amsterdam, Amsterdam, the Netherlands
*Shared senior authors

Correspondence:
R.E. van Kesteren: ronald.van.kesteren@vu.nl
M.C. van den Oever: michel.vanden.oever@vu.nl

Abstract

Patients with Alzheimer's disease (AD) initially show temporally-graded retrograde amnesia, which gradually progresses into more severe retrograde amnesia. Although mouse models of AD have provided insight into neurobiological mechanisms contributing to impaired formation and retrieval of new memories, the process underlying the progressive loss of remote memories in AD has remained elusive. Here, we demonstrate age-dependent remote memory decline in APP/PS1 mice, which coincides with progressive hyperexcitability of parvalbumin (PV) interneurons in the medial prefrontal cortex (mPFC). Analysis of Fos expression showed that the remote memory deficit is not mirrored by changes in reactivation of memory-encoding neurons, so-called engram cells, nor PV interneuron (re)activation, in the mPFC. However, inhibitory input is enhanced onto engram cells compared to non-engram cells specifically in APP/PS1 mice. Our data indicate that age-dependent remote memory impairment in APP/PS1 mice is due to increased innervation of cortical engram cells by hyperexcitable PV interneurons, suggesting that dysfunctional inhibitory microcircuits in the neocortex mediate progressive retrograde amnesia in AD.

Introduction

Alzheimer's disease (AD) is the most prevalent form of dementia and is characterized by amnesic cognitive impairment (Knopman et al., 2021). Specifically, patients with AD initially experience anterograde and temporally-graded retrograde amnesia, i.e., an inability to form new memories and retrieve recently acquired memories (hours-to-days-old). As the disease progresses, memory impairments become more profound, resulting in severe retrograde amnesia, involving the loss of more remote memories (months-to-years-old) (El Haj et al., 2015). The pathological hallmarks of the disease, neuritic plaques containing amyloid beta and neurofibrillary tangles composed of hyperphosphorylated tau, have been extensively studied to develop therapeutic interventions. Although some amyloid-targeting therapies are efficient in reducing the pathology and have recently been approved for the treatment of AD, cognitive effects of such treatments remain minimal or absent (Avgerinos et al., 2024; Li et al., 2023). Since memory loss is one of the earliest symptoms in AD and the most dehumanizing, it is important to understand its underlying mechanisms to identify new therapeutic targets that can also improve cognition or delay cognitive decline.

Memories are stored in the brain by sparse populations, or ensembles, of so-called engram cells (Josselyn & Tonegawa, 2020). These learning-activated neurons undergo structural, physiological and molecular changes to encode, store and retrieve specific memories (Josselyn et al., 2015). While initial formation and retrieval of contextual memories is hippocampus-dependent (Liu et al., 2012), memory persistence depends on memory retrieval by neocortical regions (Frankland & Bontempi, 2005). Specifically, engram cells in the medial prefrontal cortex (mPFC) are necessary for remote (> 2-week-old), but not recent (< 1-week-old), contextual memory expression in mice (Kitamura et al., 2017; Matos et al., 2019). The recruitment of neurons into an engram ensemble depends on their intrinsic excitability at the moment of learning, i.e., neurons with relatively higher excitability have a higher chance to become part of an engram (Yiu et al., 2014; Zhou et al., 2009).

Both AD patients and mouse models of AD exhibit changes in neuronal excitability (Celone et al., 2006; Dickerson et al., 2005; Palop et al., 2007). Prior to cognitive symptoms, individuals genetically at risk for AD already show increased hippocampal activation compared to non-carriers (Filippini et al., 2009). Similarly, APP23xPS45 mice show early changes in hippocampal neuron excitability before the presence of amyloid plaques (Busche and Konnerth 2015). These alterations in excitability could potentially affect memory allocation to neurons upon memory encoding and/or engram reactivation during memory retrieval, and might thereby contribute to memory loss in AD. Indeed, APP/PS1 mice show deficits in recent memory retrieval (24 h after training) prior to amyloid plaque onset (Roy et al., 2016). Interestingly, the same study reported that memory recall could be induced upon optogenetic activation of the hippocampal engram, pointing to a memory retrieval deficit in the absence of artificial engram stimulation. It remains unknown whether remote memory formation and retrieval are similarly affected, and if so, whether altered memory engram function in the mPFC is involved.

Inhibitory interneurons play an important role in memory processing and engram function. Parvalbumin (PV) and somatostatin (SST)-expressing interneurons determine the size of an engram ensemble via inhibition of surrounding (non-engram) neurons (Morrison et al., 2016; Stefanelli et al., 2016). Moreover, SST neurons in the mPFC have been implicated in the encoding and expression of fear memory (Cummings et al., 2022;

Cummings & Clem, 2020). Of relevance to this is that APP/PS1 mice present an early hyperexcitability of PV interneurons in the hippocampal CA1 at 4 months of age, which precedes pyramidal cell hyperexcitability, as well as the presence of amyloid plaques. Interestingly, chronic chemogenetic inhibition of hyperexcitable PV neurons subsequently rescues spatial memory function and precludes pyramidal cell hyperexcitability (Hijazi et al., 2020). Additionally, hippocampal SST cell dysfunction, characterized by axon loss and impairment of structural plasticity of dendritic spines, has been observed in APP/PS1 mice starting around 5 months of age (Schmid et al., 2016). These findings suggest that early interneuron dysfunction may contribute to network instability and memory deficits in AD.

Here, we investigated whether remote memory function and excitability of PV and SST interneurons are altered in the mPFC of APP/PS1 mice. Furthermore, we determined whether changes in neuronal excitability affect the size, cellular composition and reactivation of the mPFC engram ensemble that supports memory persistence. We show that age-dependent remote memory decline in APP/PS1 mice coincides with progressive hyperexcitability of PV, but not SST, cells in the mPFC. This remote memory deficit is not mirrored by changes in the PV cell composition or reactivation of the engram ensemble in the mPFC. However, our data point to increased inhibitory PV cell input onto engram cells compared to non-engram cells specifically in APP/PS1 mice, suggesting that remote memory engrams in the mPFC are impaired in APP/PS1 mice as a result of altered inhibitory synaptic transmission in engram cells, rather than changes in engram composition or size.

Results

Progressive remote memory decline in APP/PS1 mice

We first determined whether remote memory is affected in APP/PS1 mice using contextual fear conditioning (CFC). We previously found that recent fear memory (1-day-old) is impaired in APP/PS1 mice compared to wild-type (WT) littermates at 12 weeks of age (Végh et al., 2014) We therefore subjected 12-week-old APP/PS1 mice and their WT littermates to CFC and 4 weeks later, at an age of 16 weeks, remote memory was assessed by re-exposing the mice to the FC context. Freezing levels of APP/PS1 mice did not differ compared with WT controls (**Fig. 1a + b**). However, when APP/PS1 mice were trained at 16 weeks old and tested at 20 weeks old, we observed reduced freezing compared to WT littermates (**Fig. 1a + c**). Hence, APP/PS1 mice develop a remote memory deficit between 16 and 20 weeks of age, following an initial impairment of recent memory at 12 weeks of age (Végh et al., 2014).

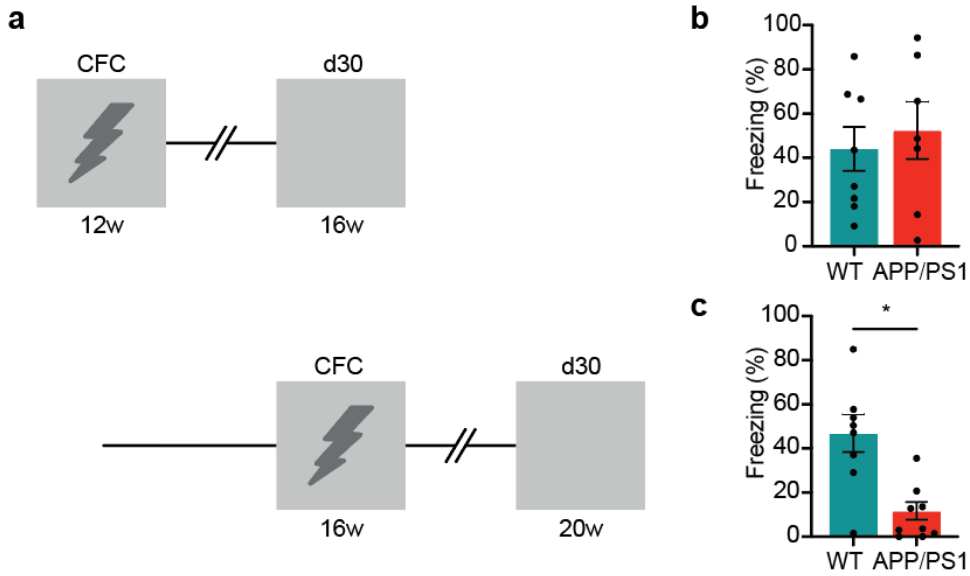

Fig. 1: Progressive remote memory decline in APP/PS1 mice. a. Experimental design. WT and APP/PS1 mice underwent contextual fear conditioning (CFC) at 12 and 16 weeks of age, and memory retrieval 30 days later at 16 weeks and 20 weeks of age, respectively. **b.** At 16 weeks old, APP/PS1 mice did not differ in freezing levels during memory retrieval compared to WT controls. Unpaired t-test: $t_{13} = 0.52$, $p = 0.61$, WT ($n = 8$), APP/PS1 ($n = 7$). **c.** At 20 weeks old, APP/PS1 mice showed reduced freezing levels during memory retrieval compared to WT controls. Unpaired t-test: $t_{15} = 3.88$, $*p = 0.002$, WT ($n = 8$), APP/PS1 ($n = 9$). Graphs show mean ± s.e.m.

<u>APP/PS1 mice show an age-dependent increase in PV interneuron excitability</u>

To determine whether changes in remote memory correlate with alterations in neuronal excitability, whole-cell patch-clamp recordings were performed in acute brain slices containing the mPFC (**Fig. 2a**). To visualize PV neurons, APP/PS1 mice were crossed with PV-Cre transgenic mice to generate APP/PS1 PV-Cre mice, which were subsequently crossed with $R26^{Al14+}$ mice to create APP/PS1-PV-Cre-tdTomato and PV-Cre-tdTomato (control) mice. Recordings were made from PV interneurons and pyramidal neurons in the prelimbic subregion of the mPFC. At 16 weeks of age, PV cell resting membrane potential, rheobase and action potential frequency in response to increasing current injections were unaltered in APP/PS1-PV-Cre-tdTomato mice compared to controls (**Fig. 2b-e**). We detected only a decrease in membrane capacitance in PV cells of APP/PS1 mice (**Supplementary table 1**). At this age, pyramidal cells in the mPFC of APP/PS1 mice also showed no alterations in resting membrane potential and action potential frequency (**Fig. 2f-i**). However, pyramidal cells exhibited a decrease in rheobase (**Fig. 2f**) as well as an increased action potential halfwidth (**Supplementary table 2**).

Contrary to 16 weeks of age, action potential frequency in PV cells was enhanced in response to increasing current injections (**Fig. 2j-m**) in APP/PS1 mice compared to WT controls at 20 weeks of age. No changes were observed in resting membrane potential and rheobase (**Fig. 2n-q**) at this age. Similar to 16-week-old mice, pyramidal cells in 20-week-old APP/PS1 mice showed a decrease in rheobase, but no alterations in resting membrane potential and action potential frequency (**Fig. 2n-q**). Action potential halfwidth of pyramidal cells was not altered in 20-week-old APP/PS1 mice (**Supplementary table 4**).

Somatostatin (SST) interneurons showed no changes in excitability or membrane properties at 20 weeks of age (**Supplemental Fig. 1; Supplemental table 5**). Thus, although mPFC PV and pyramidal cells are both affected in APP/PS1 mice, only the development of

PV cell hyperexcitability, and not of SST or pyramidal cells, mirrors the progressive decline in remote memory retrieval.

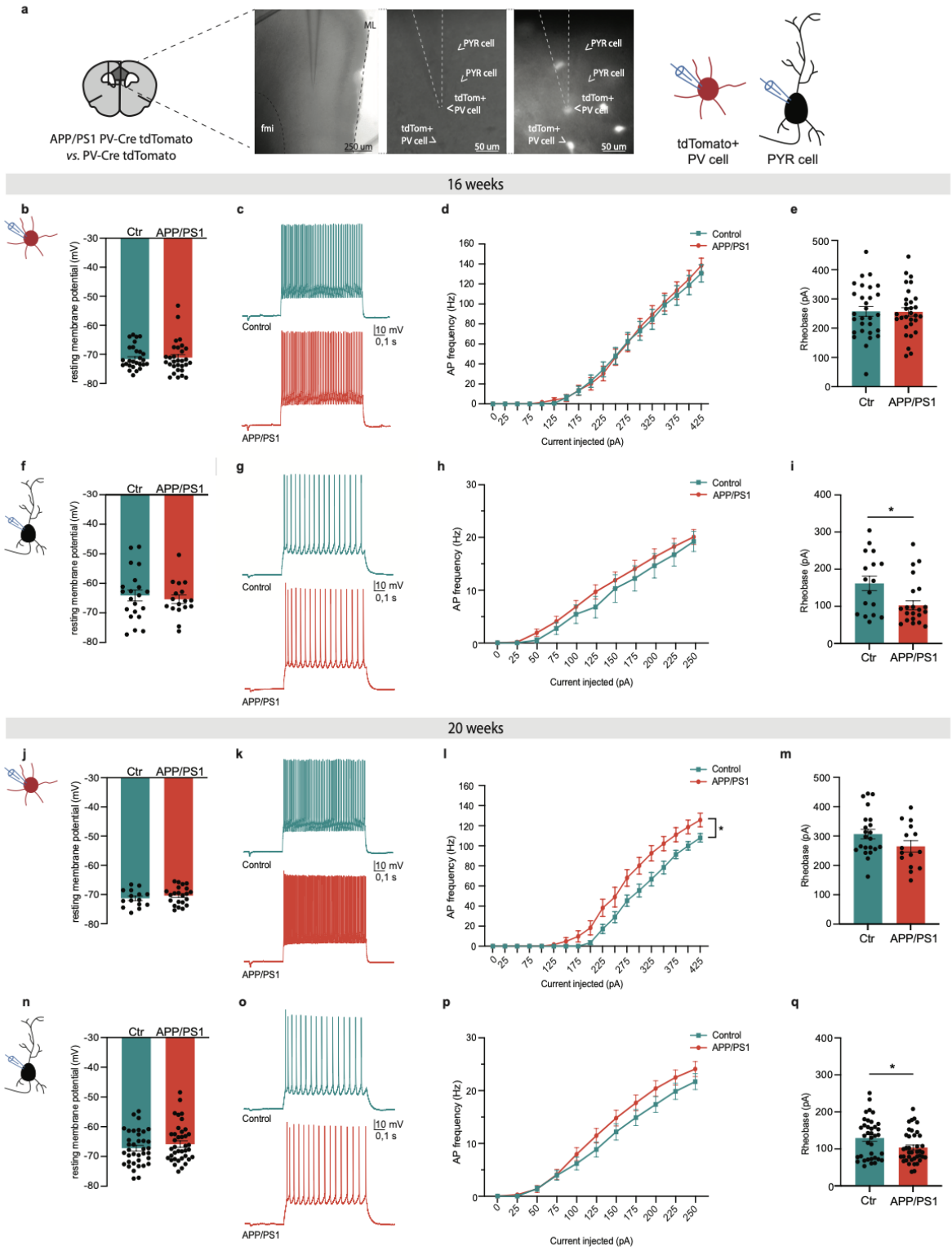

Fig. 2: APP/PS1 mice show an age-dependent increase in PV interneuron excitability. **a.** Schematic coronal brain section indicating the mPFC prelimbic region in dark grey, where tdTomato^{+} parvalbumin (PV) cells and pyramidal (PYR) cells were recorded in APP/PS1 PV-Cre tdTomato (APP/PS1) and PV-Cre tdTomato (control) mice. Representative differential interference contrast images (left) and a corresponding fluorescent image (right). fmi= forceps minor of the corpus callosum. ML= midline. Recordings were performed in 16 (**b-i**) and 20 (**j-q**) week-old mice. **b**. Resting membrane potential was unaltered in PV cells at 16 weeks of age. Mann-Whitney test: U = 433 , p = 0.98, n = 29/30 cells, N = 4 mice/genotype. Ctr= control. **c**. Action potential (AP)

163 firing of PV cells upon a depolarizing current step (250 pA). **d.** AP frequency in PV cells in response to 0-425 pA
164 depolarizing current steps did not differ between genotypes. Two-way repeated measures ANOVA *genotype x*
165 *current* $F_{(10,390)}$ = 0.44, p = 0.93, n = 29/30 cells, N = 4 mice/genotype. **e.** Rheobase was unchanged in PV cells.
166 Unpaired t-test: t_{57} = 0.08, p = 0.93, n = 29/30 cells, N = 4 mice/genotype. Ctr= control. **f**. Resting membrane
167 potential of PYR cells did not differ between genotypes. Unpaired t-test: t_{36} = 0.51, p = 0.61, n = 17/21 cells
168 from N = 4/6 control vs. APP/PS1 mice, respectively. Ctr= control. **g.** AP firing of PYR cells upon a depolarizing
169 current step (250 pA). **h.** AP frequency in PYR cells in response to 0-250 pA depolarizing current steps did not
170 differ between genotypes. Two-way repeated measures ANOVA *genotype x current* $F_{(10,370)}$ = 0.25, p = 0.99, n =
171 17/21 from N = 4/6 control vs. APP/PS1 mice, respectively. **i.** APP/PS1 mice show a lower rheobase in PYR cells.
172 Mann-Whitney test: U = 111, *p = 0.048, n = 17/21 cells from N = 4/6 control vs. APP/PS1 mice, respectively.
173 Ctr= control. **j**. Resting membrane potential was unaltered in PV cells at 20 weeks of age. Unpaired t-test: t_{35} =
174 0.93, p = 0.36, n = 22/15 cells from N = 6/7 control and APP/PS1 mice, respectively. Ctr= control. **k.** AP firing of
175 PV cells upon a depolarizing current step (250 pA). **l.** APP/PS1 mice show an increased AP frequency in PV cells
176 in response to 0-425 pA depolarizing current steps. Two-way repeated measures ANOVA *genotype x current*
177 $F_{(17,595)}$ = 4.05, *p < 0.0001, n = 22/15 cells, N = 6/7 control and APP/PS1 mice, respectively. **m**. Rheobase was
178 unchanged in PV cells. Unpaired t-test: t_{35} = 1.67, p = 0.10, 22/15 cells, N = 6/7 control and APP/PS1 mice,
179 respectively. Ctr= control. **n.** Resting membrane potential of PYR cells did not differ between genotypes.
180 Unpaired t-test: t_{74} = 0.92, p = 0.36, n = 37/39 cells, N = 9 mice/genotype. Ctr= control. **o**. AP firing of PYR cells
181 upon a depolarizing current step (250 pA). **p**. AP frequency in PYR cells in response to 0-250 pA depolarizing
182 current steps did not differ between genotypes. Two-way repeated measures ANOVA *genotype x current*
183 $F_{(10,740)}$ = 1.80, p = 0.08, n = 37/39 cells, N = 9 mice/genotype. **q.** APP/PS1 mice show a decrease in PYR cell
184 rheobase. Unpaired t-test: t_{74} = 2.34, *p = 0.022, n = 37/39 cells, N = 9 mice/genotype. Ctr= control. Graphs
185 show mean ± s.e.m.
186
187 <u>Size and reactivation of the mPFC engram ensemble are unaffected in APP/PS1 mice</u>
188 We previously demonstrated that reactivation of mPFC engram cells is required for remote
189 memory retrieval one month after CFC using a viral-TRAP (targeted recombination in active
190 populations) engram tagging approach (Matos et al., 2019). Here, we used the same
191 technique to determine whether remote memory deficits in APP/PS1 mice at 20 weeks of
192 age are reflected by alterations in properties and reactivation of the mPFC engram
193 ensemble. Viral-TRAP allowed hydroxytamoxifen (4TM)-controlled permanent expression of
194 mCherry in activated neurons based on activation of the *Fos* promoter (Cruz et al., 2013;
195 Guenthner et al., 2013) (**Fig. 3a**). Following viral-TRAP injection into the mPFC, APP/PS1 mice
196 and their WT control littermates were subjected to CFC at either 12 or 16 weeks of age,
197 after which CFC-activated cells were permanently labeled with mCherry upon 4TM injection.
198 Four weeks later, at either 16 weeks or 20 weeks of age, remote memory retrieval was
199 assessed (**Fig. 3b**). We confirmed that APP/PS1 mice have a remote memory deficit at 20
200 weeks, but not at 16 weeks, of age (**Supplemental Fig. 2**).
201 Mice were perfused 90 min after the retrieval test, followed by
202 immunohistochemical staining of mPFC sections for Nissl (general neuronal marker), PV, and
203 Fos (representing neurons activated during memory retrieval; **Fig. 3c; 3k**). The percentage of
204 PV^+ (**Fig. 3d+l**), $mCherry^+$ (**Fig. 3e+m**), and Fos^+ (**Fig. 3f+n**) neurons did not differ between
205 control and APP/PS1 mice at either 16 or 20 weeks of age.
206 Reactivation of $mCherry^+$ engram cells was assessed by examining colocalization of
207 Fos^+ and $mCherry^+$ cells. In line with our previous findings (Matos et al., 2019), both control
208 and APP/PS1 mice showed enhanced colocalization of Fos with $mCherry^+$ cells
209 ($mCherry^+/Nissl^+$) compared to $mCherry^-$ cells ($mCherry^-/Nissl^+$) at 16 weeks of age, pointing
210 to preferential reactivation of engram cells when remote memory retrieval is still intact (**Fig.**
211 **3g**). Surprisingly, we observed similar preferential colocalization of Fos^+ and $mCherry^+$ cells
212 in both genotypes at 20 weeks of age (**Fig. 3o**). Thus, while APP/PS1 mice showed impaired

remote memory expression when they are 20 weeks old, reactivation of the engram ensemble in the mPFC seemed unaffected.

PV interneuron (re)activation is unaffected in APP/PS1 mice

Next, we quantified colocalization of PV^+ and $mCherry^+$ cells, representing the number of PV cells initially recruited to the mPFC engram ensemble (**Fig. 3h+p**). In both age groups and genotypes, PV^+ cells were overrepresented in the $mCherry^+$ compared with $mCherry^-$ population. Furthermore, we studied the overlap between Fos^+ and $PV^+/mCherry^-$ cells, reflecting the number of activated non-tagged PV cells during memory retrieval. We did not find differences between genotypes at 16 and 20 weeks of age (**Fig. 3i+q**), but in all groups, PV^+ cells were less likely to be activated than PV^- cells during memory retrieval, in contrast to the preferential activation (and tagging) of PV^+ cells during training.

Finally, we quantified the colocalization of PV^+, Fos^+ and $mCherry^+$ cells, representing PV cells that were tagged during CFC and reactivated during remote memory expression. Strikingly, the percentage of Fos^+ cells was higher in the $PV^+/mCherry^+$ population than the $PV^+/mCherry^-$ population in APP/PS1 and control mice at both ages (**Fig. 3j+r**). This indicates that tagged PV^+ cells were preferentially reactivated during remote memory expression, in contrast to the reduced activation of PV^+ cells that were not part of the engram population. However, this did not differ between genotypes in 16- and 20-week-old mice. Thus, while PV cells are hyperexcitable at 20 weeks of age in APP/PS1 mice, they do not seem to be differently recruited during memory encoding, nor (re)activated during remote memory retrieval.

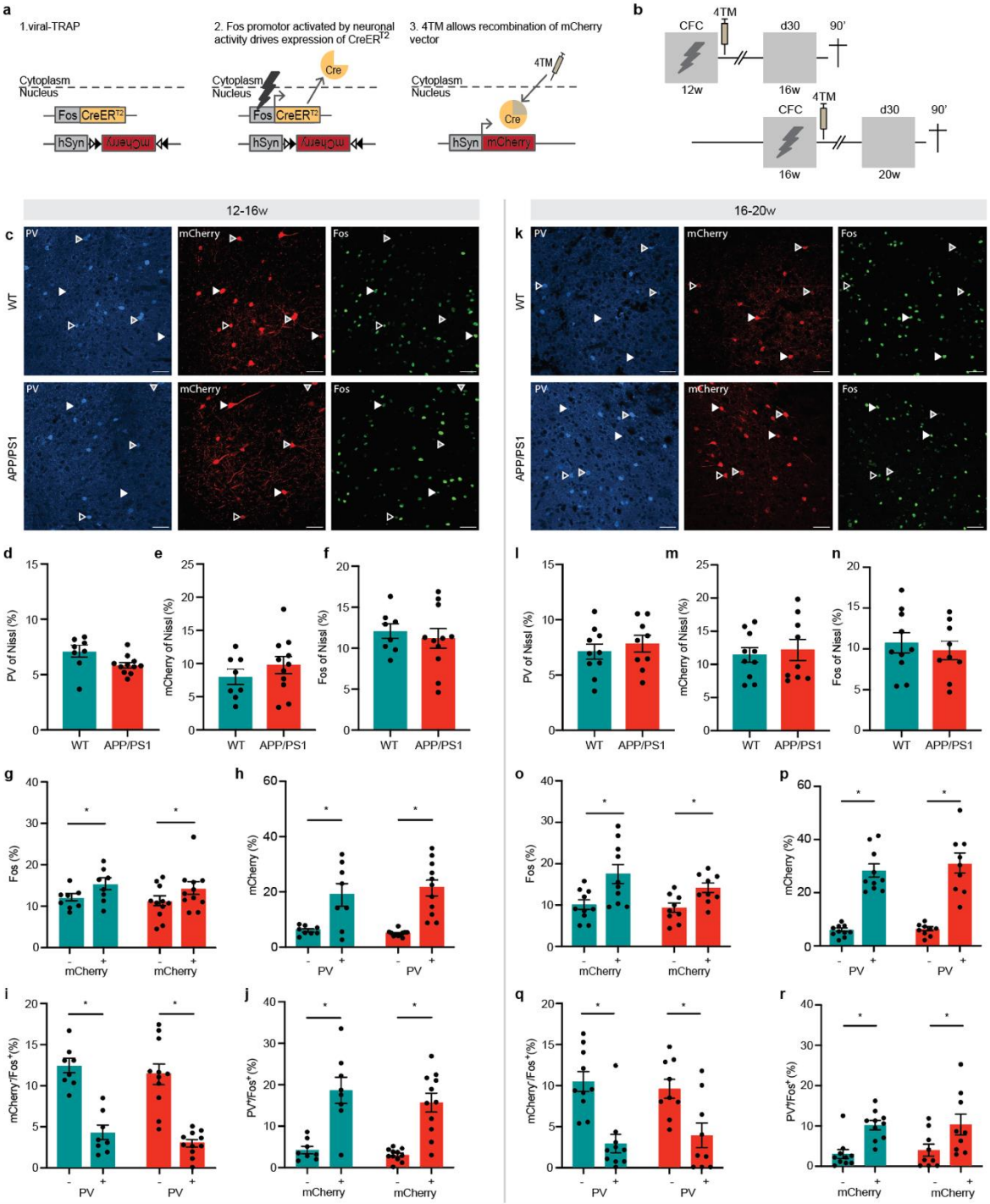

Fig. 3: Size and reactivation of the mPFC engram ensemble, as well as PV interneuron (re)activation, are unaffected in APP/PS1 mice. a. Schematic representation of the viral-TRAP method. A viral cocktail of AAV-Fos::CreER^{T2} and Cre-dependent AAV-hSyn::DIO-mCherry were injected into the mPFC, allowing irreversible expression of mCherry upon neuronal activity and systemic injection of 4-hydroxytamoxifen (4TM). **b.** Schematic timeline depicting CFC and engram tagging at 12 weeks (WT n = 8, APP/PS1 n = 11 mice) or 16 weeks (WT n = 10, APP/PS1 n = 9 mice) old. On d30 after training, mice underwent a remote memory test at 16 or 20 weeks old and were perfused 90 min later. **c.** Representative images at 12-16w showing PV$^+$, mCherry$^+$ and Fos$^+$ cells in WT (top row) and APP/PS1 (bottom row) mice. Nissl staining (general neuronal marker) is not shown. White arrowheads indicate reactivated neurons (Fos$^+$/mCherry$^+$ cells). Gray arrowheads indicate PV cells part of the engram (PV$^+$/mCherry$^+$ cells). Empty arrowheads indicate reactivated PV neurons (Fos$^+$/mCherry$^+$/PV$^+$ cells). Scale bar = 50 µm. Colocalization of cell-type markers is shown for 16 (**d-j**) and 20 (**l-r**) week-old mice **d.** Percentage of PV cells did not differ between genotypes. Unpaired t-test: t_{17} = 2.04, p =

0.06. **e.** Percentage of mCherry$^+$ cells did not differ between genotypes. Unpaired t-test: t_{17} = 1.02, p = 0.32. **f**. Percentage of Fos$^+$ cells did not differ between genotypes. Unpaired t-test: t_{17} = 0.53, p = 0.60. **g**. Fos colocalization with mCherry$^+$ cells (mCherry$^+$/Nissl$^+$) was enhanced compared to mCherry$^-$ cells (mCherry$^-$/Nissl$^+$) in WT and APP/PS1 mice. Two-way repeated measure ANOVA *cell population*: $F_{(1,17)}$ = 16.3, *p = 0.0009. Post-hoc Bonferroni test: Control *p = 0.028; APP/PS1 *p = 0.016. **h.** Percentage of PV$^+$ cells in the mCherry$^+$ population was higher than in the mCherry$^-$ population for both genotypes. Two-way repeated measure ANOVA *cell population:* $F_{(1,17)}$ = 31.70, *p < 0.0001. Post-hoc Bonferroni test: WT *p = 0.010; APP/PS1 *p = 0.0003. **i.** Percentage of Fos$^+$ cells was higher in the mCherry$^-$/PV$^-$ than mCherry$^-$/PV$^+$ population. Two-way repeated measure ANOVA *cell population*: $F_{(1,17)}$ = 179.30, *p <0.0001; Post-hoc Bonferroni test: WT *p <0.0001; APP/PS1 *p <0.0001. **j**. Percentage of Fos$^+$ cells was higher in the PV$^+$/mCherry$^+$ population compared to the PV$^+$/mCherry$^-$ population in APP/PS1 and WT mice. Two-way repeated measure ANOVA *cell population:* $F_{(1,17)}$ = 50.57, *p < 0.0001; Post-hoc Bonferroni test: WT *p = 0.0002; APP/PS1 *p = 0.0002. **k**. Representative images at 16-20w showing PV$^+$, mCherry$^+$ and Fos$^+$ cells in WT (top row) and APP/PS1 (bottom row) mice. **l**. Percentage of PV cells did not differ between genotypes. Unpaired t-test: t_{17} = 0.67, p = 0.51. **m**. Percentage of mCherry$^+$ cells did not differ between genotypes. Unpaired t-test: t_{17} = 0.42, p = 0.68. **n**. Percentage of Fos$^+$ cells did not differ between genotypes. Unpaired t-test: t_{17} = 0.55, p = 0.59. **o**. Fos colocalization with mCherry$^+$ cells (mCherry$^+$/Nissl$^+$) was enhanced compared to mCherry$^-$ cells (mCherry$^-$/Nissl$^+$) in WT and APP/PS1 mice. Two-way repeated measure ANOVA *cell population*: $F_{(1,17)}$ = 56.41, *p < 0.0001. Post-hoc Bonferroni test: WT *p < 0.0001; APP/PS1 *p = 0.002. **p**. Percentage of PV$^+$ cells in the mCherry$^+$ population was higher than in the mCherry$^-$ population for both genotypes. Two-way repeated measure ANOVA *cell population:* $F_{(1,17)}$ = 82.15, *p < 0.0001. Post-hoc Bonferroni test: WT control *p < 0.0001; APP/PS1 *p < 0.0001. **q**. Percentage of Fos$^+$ cells was higher in the mCherry$^-$/PV$^-$ than mCherry$^-$/PV$^+$ population. Two-way repeated measure ANOVA *cell population*: $F_{(1,17)}$ = 39.15, p <0.0001; Post-hoc Bonferroni test: WT *p = 0.0001; APP/PS1 *p = 0.004. **r**. Percentage of Fos$^+$ cells was higher in the PV$^+$/mCherry$^+$ population compared to the PV$^+$/mCherry$^-$ population in APP/PS1 and WT mice. Two-way repeated measure ANOVA *cell population:* $F_{(1,17)}$ = 17.38, *p = 0.001. Post-hoc Bonferroni test: WT *p = 0.010; APP/PS1 *p = 0.031. Graphs show mean ± s.e.m.

<u>Perisomatic PV labelling is increased on engram cells in 20-week-old APP/PS1 mice</u>

Neocortical PV interneurons predominantly synapse onto the soma, proximal dendrites and axon initial segment of other neurons to control their output (Tremblay et al., 2016). Therefore, we hypothesized that differential PV innervation of engram versus non-engram cells might underly the remote memory deficit in 20-week-old APP/PS1 mice. As a first step to address this, we measured the surface area of PV$^+$ labelling in close proximity to the soma of mCherry$^+$/PV$^-$ cells and compared this to neighboring mCherry$^-$/PV$^-$ cells (**Fig. 4**) (Trouche et al., 2013). In the 12–16 week groups, we found a similar amount of PV labelling around mCherry$^+$ cells compared to mCherry$^-$ cells, for both control and APP/PS1 mice (**Fig. 4a-c**). In contrast, PV labelling around mCherry$^+$ cells was enhanced compared to mCherry$^-$ cells in APP/PS1, but not in control mice in the 16–20 week groups (**Fig. 4d-f**), suggesting that inhibitory input may be selectively enhanced in mPFC engram cells of 20-week-old APP/PS1 mice.

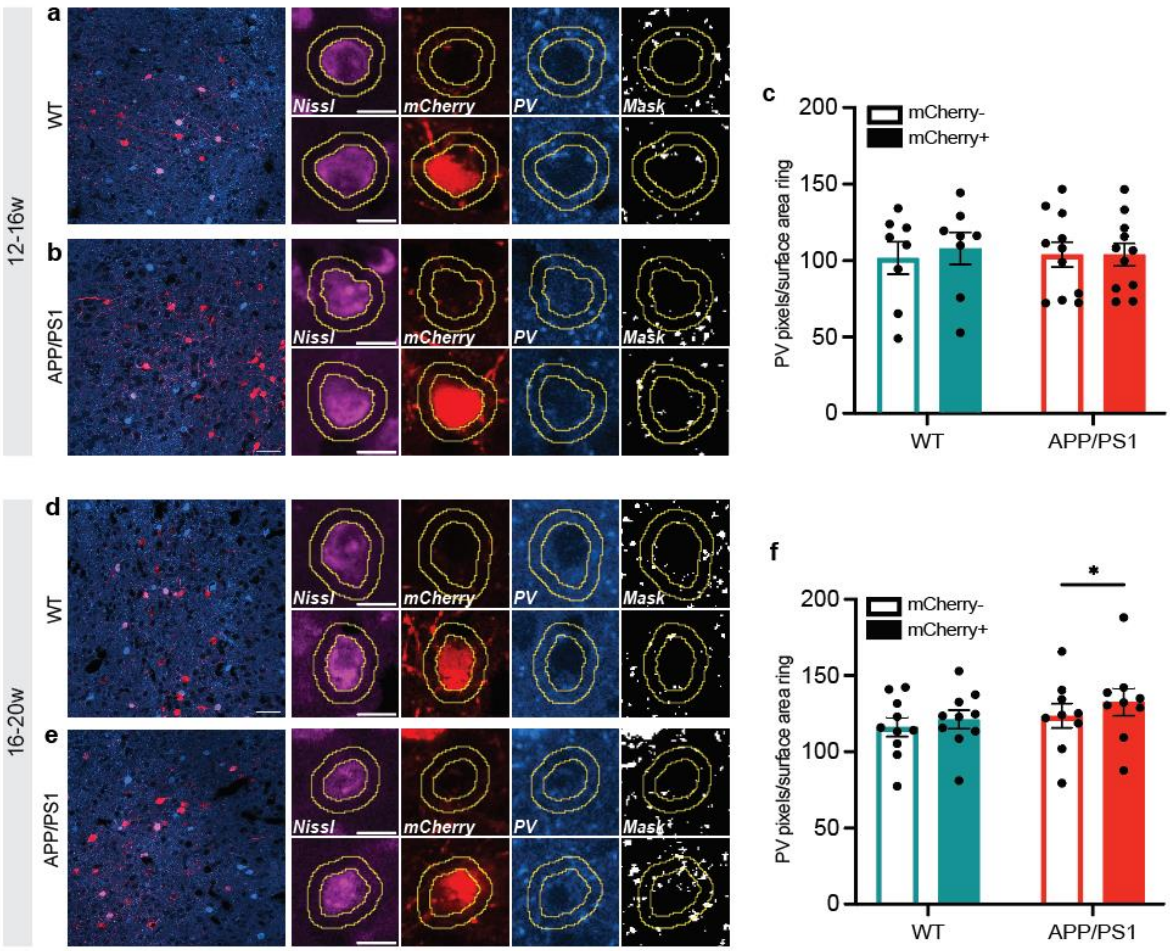

Fig. 4: Perisomatic PV labelling is increased on engram cells in 20-week-old APP/PS1 mice. a-b. Left: Representative image of WT (a) and APP/PS1 (b) mice from the 12-16 week groups showing PV staining and mCherry$^+$ cells in the mPFC. Scale bar = 50 µm. Right: Examples of a mCherry$^-$ (top row) and mCherry$^+$ (bottom row) cell. Soma outline is based on Nissl. PV signal was masked and measured inside the ring surrounding the soma. Scale bar = 10 µm. **c.** PV labelling around mCherry$^+$ cells did not differ from mCherry$^-$ cells in WT and APP/PS1 mice. Two-way repeated measure ANOVA *cell population:* $F_{(1,17)} = 2.25$; $p = 0.15$; WT ($n = 8$), APP/PS1 ($n = 11$) **d.** Left: Representative image of WT (d) and APP/PS1 (e) mice from the 16-20 week groups showing PV staining and mCherry$^+$ cells in the mPFC. Scale bar = 50 µm. Right: Examples of a mCherry$^-$ (top row) and mCherry$^+$ (bottom row) cell. Soma outline is based on Nissl. PV signal was masked and measured inside the ring surrounding the soma. Scale bar = 10 µm. **f**. An increased amount of PV labelling around mCherry$^+$ cells was found compared to mCherry$^-$ cells in APP/PS1 mice but not control mice. Two-way repeated measure ANOVA *cell population*: F(1,17) = 21.74 ; $*p = 0.0002$. Post-hoc Bonferroni test: APP/PS1 mCherry+ vs. mCherry- $*p = 0.0015$. Graphs show mean ± s.e.m.

<u>Engram cells of 20-week-old APP/PS1 mice receive increased inhibitory input</u>

We next aimed to confirm that inhibitory synaptic transmission is altered in engram cells of APP/PS1 mice using whole-cell patch-clamp electrophysiology. Viral-TRAP was used to permanently label CFC-activated engram cells in the mPFC and 4 weeks later, at 20 weeks of age, we subjected mice to a memory retrieval session, after which we immediately generated acute brain slices to measure spontaneous inhibitory and excitatory postsynaptic currents (sIPSCs and sEPSCs, respectively) from mCherry$^+$, and neighboring mCherry$^-$, pyramidal cells (**Fig. 5a-d**). A two-way repeated measure ANOVA revealed an interaction effect between genotype and cell-type for sIPSC frequency. Post-hoc analysis confirmed that in APP/PS1 mice, sIPSC frequency was increased in mCherry$^+$ cells compared to neighboring

mCherry$^-$ cells, which was not observed in WT control mice (post-hoc Bonferroni test: APP/PS1 mCherry$^+$ *vs.* mCherry$^-$ p = 0.011) (**Fig. 5e**). The sIPSC amplitude did not differ between mCherry$^+$ and mCherry$^-$ cells in both APP/PS1 and WT mice (**Fig. 5f**). Finally, we measured sEPSC frequency and amplitude onto mCherry$^+$ and mCherry$^-$ cells. For sEPSC frequency, a two-way repeated measure ANOVA did not detect an interaction effect but revealed a main effect of cell population, without a significant post-hoc difference, indicating that spontaneous excitatory input onto engram cells was enhanced independent of genotype (**Fig. 5g**). Similar to sIPSC amplitude, there was no difference in sEPSC amplitude between mCherry$^+$ and mCherry$^-$ cells (**Fig. 5h**). Hence, excitatory drive onto mPFC engram cells is modestly enhanced in control and APP/PS1 mice, whereas inhibitory input onto the same cells is selectively augmented in APP/PS1 mice.

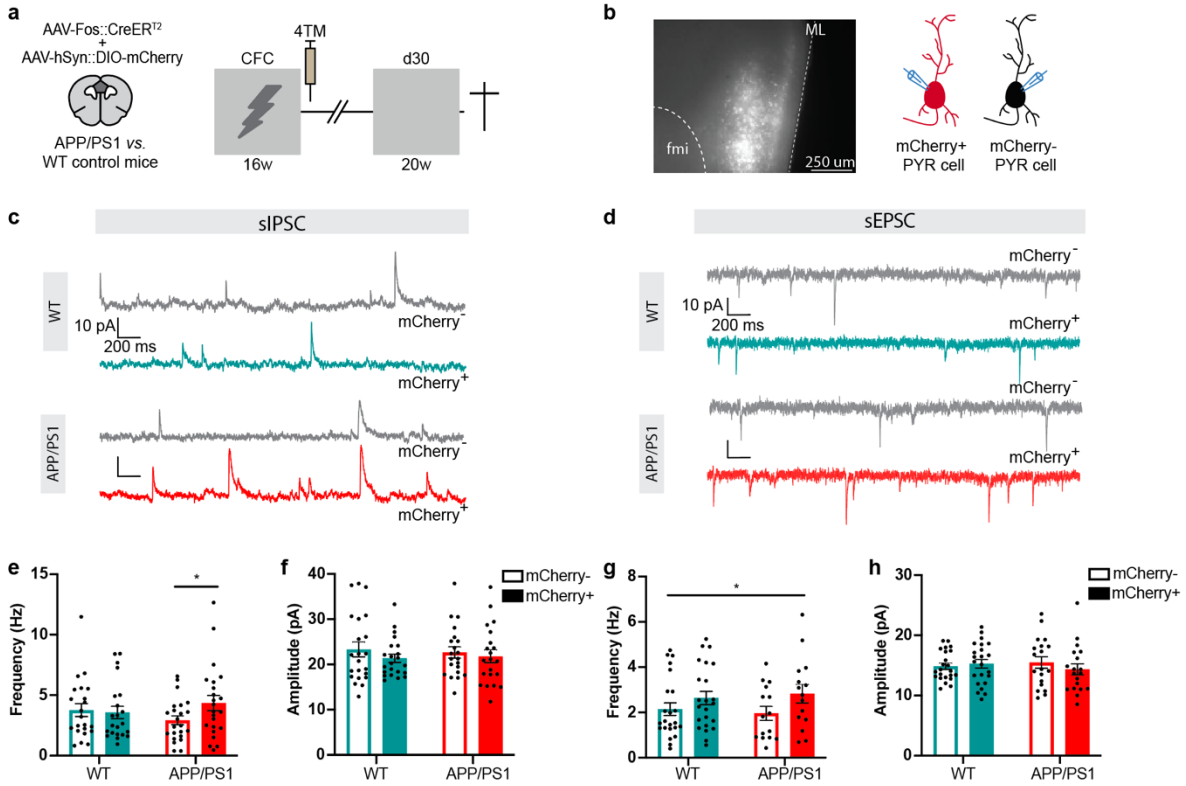

Fig. 5: Engram cells of 20-week-old APP/PS1 mice receive increased inhibitory input. a. Coronal brain section indicating the mPFC region (dark grey) where AAV-Fos::CreER^{T2} and Cre-dependent AAV-hSyn::DIO-mCherry were injected. Mice underwent CFC at 16 weeks old and engram cells were tagged. Thirty days after CFC, mice were re-exposed to the training context and then immediately sacrificed for whole-cell patch-clamp electrophysiology. **b**. Left: Representative image showing labeled mCherry$^+$ engram cells in the mPFC. Right: recordings were made from mCherry$^+$ and mCherry$^-$ pyramidal cells. **c**. Example sIPSC traces of mCherry$^+$ and mCherry$^-$ for WT control and APP/PS1 mice **d**. Example sEPSC traces of mCherry$^+$ and mCherry$^-$ cells for WT and APP/PS1 mice **e.** Frequency of sIPSCs differed between mCherry$^+$ and mCherry$^-$ cells in APP/PS1, but not WT, mice. Two-way repeated measure ANOVA *genotype x cell-type* $F_{(1,43)}$ = 5.44, *p = 0.024. Post-hoc Bonferroni APP/PS1 mCherry$^+$ *vs.* mCherry$^-$ *p = 0.011. n = 22 per cell-type from N = 6 WT mice, n = 23 per cell-type from N = 7 APP/PS1 mice. **f.** sIPSC amplitude did not differ between cell-type and genotype. **g.** Frequency of sEPSCs was enhanced in mCherry$^+$ cells compared to mCherry$^-$ cells in both genotypes. Two-way repeated measure ANOVA *cell-type* $F_{(1,36)}$ = 7.26, *p = 0.011 n = 20 per cell type from N = 6 WT mice, n = 23 per cell-type from N = 7 APP/PS1 mice **h.** sEPSC amplitude did not differ between cell-type and genotype. Graphs show mean ± s.e.m.

Discussion

In this study, we demonstrate an age-dependent decline in remote memory retrieval in APP/PS1 mice, which coincides with progressive PV interneuron hyperexcitability in the mPFC. Strikingly, this remote memory deficit does not seem to be mirrored by alterations in initial activation of neurons during learning, reactivation of the engram ensemble during memory retrieval, nor (re)activation of PV cells in the mPFC, as assessed using Fos expression. Interestingly, the amount of PV labelling on engram cells was increased compared to non-engram cells in APP/PS1 mice, which was not observed in control mice. In addition, we observed enhanced spontaneous inhibitory input onto engram cells in APP/PS1 but not control mice. Together, these findings suggest that increased innervation of mPFC engram cells by hyperexcitable PV interneurons rather than alterations in engram composition is responsible for remote memory deficits in APP/PS1 mice.

APP/PS1 mice recapitulate pathological changes in AD, including amyloid beta plaque deposition, astrogliosis and microgliosis (Jackson et al., 2013; Liu et al., 2020). Here, we show that this mouse model also shows an age-dependent impairment in remote memory, mirroring the gradual loss of remote memories in AD patients. These patients initially experience anterograde and temporally-graded retrograde amnesia, which progressively develops into a more profound retrograde memory impairment (El Haj et al., 2015; Knopman et al., 2021). In line with this, we previously reported that APP/PS1 mice show recent memory deficits already at 12 weeks of age (Végh et al., 2014). Here we show that when mice are trained at 12 weeks of age and memory is assessed at a remote time point, i.e. 4 weeks later, remote memory retrieval is still unaffected. However, remote memory is impaired when APP/PS1 mice are trained at 16 weeks old and memory retrieval is evoked one month later. Hence, whereas initially only recent memory is affected in APP/PS1 mice, i.e., mimicking early temporally-graded retrograde amnesia in patients, remote memory can no longer be retrieved at a later age, resembling the more severe retrograde amnesia, as observed in late-stage AD patients. It is remarkable that APP/PS1 mice can acquire a remote memory at an age at which recent memory retrieval is already affected. We speculate that in 12-week-old APP/PS1 mice memory allocation to hippocampal and cortical engram cells is still intact, in line with other studies (Perusini et al., 2017; Roy et al., 2016). This may be sufficient to promote consolidation of the memory into cortical engram circuits resulting in formation of a remote memory, independent of the recent memory retrieval deficit.

To our knowledge, remote CFC memory has not been previously studied in APP/PS1 mice before. Contrary to our results, however, 5xFAD mice show a remote memory deficit (30 days after CFC) prior to recent memory deficit (1 day after CFC) before 4 months of age (Kimura & Ohno, 2009). Given the slower development of remote memory impairment compared with recent memory loss in AD patients, APP/PS1 mice may serve as a more suitable model for investigating memory decline in AD. Although extrapolations to human AD should be made with caution, the distinction between recent and remote memory mechanisms in mice could provide useful information for targeting early- and late-stage memory decline in humans more specifically.

At 20 weeks of age, APP/PS1 mice exhibit PV cell hyperexcitability in the mPFC, which was not present in 16-week-old animals, thereby mirroring the development of remote memory dysfunction. The hyperexcitability is specific to PV expressing interneurons, as the same change was not observed in SST cells. Differences in intrinsic excitability are

known to affect the probability that a neuron is recruited to an engram (Yiu et al., 2014; Zhou et al., 2009) and PV interneurons control the size of an engram (Morrison et al., 2016). However, we found that both the size and PV cell content of the mPFC engram ensemble did not differ between APP/PS1 and control mice, suggesting that memory allocation is not affected. Similarly, memory allocation to neurons in the hippocampal dentate gyrus in APP/PS1 mice is not altered even though recent memory retrieval is impaired (Perusini et al., 2017; Roy et al., 2016). This points to a recent and remote memory retrieval problem in APP/PS1 mice, as opposed to an encoding deficit. However, in contrast to reduced DG engram reactivation in APP/PS1 mice during recent memory expression (Perusini et al., 2017; Roy et al., 2016), reactivation of the mPFC engram during remote retrieval did not seem to differ between APP/PS1 and control mice in our study, suggesting that the remote memory deficit is caused by a different mechanism.

Surprisingly, at 20 weeks of age, the percentage of activated PV cells during memory retrieval was not affected in APP/PS1 mice, despite the overall PV cell hyperexcitability in the mPFC. However, in both control and APP/PS1 mice, and independent of age, PV cells appear to be inhibited during remote retrieval, as activation of the non-tagged PV population was reduced compared with other non-tagged neurons. In contrast, during conditioning, PV cells were preferentially activated compared to non-PV cells in both genotypes. In line with our data, fear expression (i.e. freezing behaviour) is causally related to reduced PV interneuron activity in the mPFC (Courtin et al., 2014; Cummings & Clem, 2020). In contrast to the non-tagged PV population, we demonstrate that tagged PV cells were reactivated above chance level during remote memory retrieval in both control and APP/PS1 mice. While interneurons exhibit learning-induced molecular, structural and electrophysiological plasticity (Donato et al., 2013; Trouche et al., 2013; Wolff et al., 2014), it remains to be determined whether the subset of learning-tagged PV cells are functionally involved in remote memory expression.

Despite the lack of changes in (re)activation of PV interneurons, our data indicate that augmented inhibitory input onto engram cells in the mPFC may underlie the remote memory deficit in 20-week-old APP/PS1 mice. The concurrent increase in PV labelling around engram cells and PV cell hyperexcitability at 20 weeks, strongly suggest that the altered inhibitory drive is mediated by PV cells. Although SST cell excitability is not affected in 20-week-old APP/PS1 mice, we cannot exclude the possibility that input from SST cells or other inhibitory neurons contributes to the enhanced sIPSC frequency in mPFC engram cells. Moreover, despite the difference in inhibitory input, overall reactivation of engram cells appears unchanged in APP/PS1 mice. This paradox, where altered synaptic input does not lead to a change in engram reactivation, suggests we may not have been able to detect changes in engram function using Fos expression as a proxy for neuronal activity. Fos is a widely used tool to study neuronal activity and engram ensembles (Cruz et al., 2013), however, Fos expression does not accurately capture changes in the level of neuronal activity, nor in synchronization of activity, the latter being a key characteristic of a functional neuronal ensemble (Buzsáki, 2010; Josselyn & Tonegawa, 2020; Zhou et al., 2020). Selectively enhanced activity of shock-responsive PV cells in the retrosplenial cortex has recently been observed during subsequent freezing epochs using *in vivo* calcium imaging, and this PV ensemble dynamic is disrupted in 5xFAD mice (Park et al., 2024). The reactivated subset of PV cells in our study may reflect the shock-responsive PV ensemble and potentially regulate pyramidal engram cells firing patterns. PV interneurons are critical for the rhythmic firing of pyramidal cells (Buzsáki, 2002), which is essential for memory processes (Courtin et

al., 2014). In APP/PS1 mice, hyperexcitability of PV cells may disrupt their synchronicity and thereby the synchronous firing of other engram cells during memory retrieval, which is not captured by Fos expression. Alternatively, changes in the output of mPFC engram cells might mediate the remote memory impairment. PV interneurons are known to exert inhibition at the soma and axonal initial segment of pyramidal cells and thereby suppress their output (Somogyi et al., 1982; Veres et al., 2014). Enhanced inhibition at these sites may interfere with memory retrieval independent of the dendritic excitatory inputs that induce Fos expression. PV neurons in the mPFC have also been shown to inhibit pyramidal neurons projecting to the basolateral amygdala, and disinhibition of these pyramidal cells evokes fear expression (Courtin et al., 2014). Hence, PV cell mediated alterations in firing synchronicity and/or output of engram cells might underlie the observed remote memory deficit in APP/PS1 mice and are therefore important topics for future research. Additionally, long-range GABAergic projections of fast-spiking PV neurons in the mPFC have been identified (Lee et al., 2014) and may also contribute to remote memory impairment without altering local Fos expression.

The opposing level of activity of learning-tagged and non-tagged PV interneurons during remote memory retrieval (i.e. enhanced vs. decreased activity, respectively) may be relevant for memory expression. To determine the causal contribution of PV cell changes in APP/PS1 mice, it may thus be necessary to simultaneously manipulate both PV populations in opposite directions, i.e., stimulate non-tagged PV cells and inhibit learning-activated PV cells, or to selectively target one of these subsets. This requires use of an intersectional approach (Fenno et al., 2014). However, as in our experiments, both engram tagging (viral-TRAP) and PV labelling (PV-Cre mice) depend on Cre-mediated recombination, this presents technical challenges and remains to be addressed with novel complementary techniques in the future.

In addition to excitability changes in PV cells, we observed a significantly decreased rheobase in mPFC pyramidal cells of APP/PS1 mice at both 16 weeks and 20 weeks of age. Interestingly, an age-related decrease in rheobase in pyramidal cells has been previously reported (Popescu et al., 2021) and is associated with spatial working memory deficits (Moore et al., 2023). This suggests that pyramidal cells in young adult APP/PS1 mice show characteristics that resemble the aged brain. Whether and how the altered rheobase in mPFC pyramidal cells contributes to dysfunctional remote memory in APP/PS1 mice remains to be elucidated. Notably, we observed a right-ward shift in the AP frequency curve in response to increasing current injections in PV cells when comparing 16 and 20-week-old control mice, suggestive of an age-dependent change in PV interneuron excitability. In support of this, human studies have shown a weakening of action potentials in fast-spiking cortical interneurons with age, caused by an increase in spike halfwidth and decrease in action potential rise speed (Szegedi et al., 2024). It would be interesting to investigate whether this rightward shift continues with age and what the potential consequences might be at the engram level, in terms of memory storage and retrieval.

To conclude, we demonstrate that PV cell hyperexcitability and enhanced inhibitory input onto mPFC engram cells coincides with an age-dependent remote memory decline in an AD mouse model. Moving forward, it is important to focus on changes in network synchrony and output of cortical engram cells as potential contributors to remote memory impairment. Understanding these network dynamics and the specific cells that are affected in AD is crucial for the identification of new therapeutic targets for alleviation of memory loss in AD.

Methods

Animals

APP/PS1 mice (The Jackson Laboratory, APPswe,PSEN1de9, B6C3-Tg, stock number 004462) express a chimeric mouse/human APP gene harboring the Swedish double mutation K59N/M596L (APPswe) and a human PS1 gene harboring the exon 9 deletion (PS1dE9). Both are under control of the mouse prion promotor (MoPrP.Xho) (Jankowsky et al., 2004; Jankowsky et al., 2001; Jankowsky et al., 2003). PV-Cre mice (The Jackson Laboratory, B6.129P2-Pvalbtm1(cre)Arbr/J, stock number 017320) express Cre recombinase under the control of the endogenous parvalbumin promotor, directing Cre recombinase expression to mouse parvalbumin expressing cells. SST-Cre mice (The Jackson Laboratory, Ssttm2.1(cre)Zjh/J, stock number 013044) express Cre recombinase under the control of the endogenous somatostatin promotor, directing Cre recombinase expression to mouse somatostatin expressing cells. All mouse lines were maintained on a C57BL/6J background. Hemizygous APP/PS1 mice were crossed with hemizygous PV-Cre or SST-Cre mice to produce double-transgenic mice and single transgenic controls. APP/PS1 PV-Cre tdTomato mice were obtained by crossing APP/PS1 Parv-Cre and wild type Parv-Cre with R26AI14+ mice (The Jackson Laboratory, B6.Cg-Gt(ROSA)26Sortm14(CAG-tdTomato)Hze/J, stock number 007914). Male mice were used in all experiments and were individually housed on a 12h light/dark cycle with ad libitum access to water and food. All experiments were approved by the Netherlands Central Committee for Animal Experiments (CCD) and the animal ethical care committee (IVD) of the Vrije Universiteit Amsterdam.

AAV vectors and stereotactic micro-injections

AAV-Fos::CreER^{T2} (titer: 1.2×10^{13}) and Cre-dependent AAV-hSyn::DIO-mCherry (titer: 1.68×10^{11}) were packaged as serotype 5 virus. Prior to stereotactic micro-injections (Matos et al., 2019; Van den Oever et al., 2013), mice received Temgesic (0.1 mg per kg, RB Pharmaceuticals, UK) and were anesthetized using isoflurane. When mounted in a stereotactic frame, lidocaine (2%, Sigma-Aldrich Chemie N.V, The Netherlands) was applied topically to the skull for local analgesia. AAV mixtures of AAV-Fos:: CreER^{T2} and Cre-dependent AAV-hSyn::DIO-mCherry (ratio 1:500) were injected bilaterally in the mPFC (+ 1.8 mm AP; ±0.45 mm ML; −2.1 mm DV; relative to Bregma). For SST-Cre mice the Cre-dependent AAV-hSyn::DIO-mCherry was injected. Each hemisphere was infused with 0.5 µL virus using microinjection glass needles, connected to a 10 µL Hamilton syringe by pressure ejection with a rate of 0.1 µL/min. This was followed by an additional 5 minutes to allow for diffusion of the viral mixture. Mice remained single-housed in their home-cage for 2 weeks until the start of behavioral experiments.

Contextual fear memory

Four days prior to undergoing contextual fear conditioning (CFC), mice were handled for two consecutive days and then left undisturbed in their home. CFC training was performed in a soundproof cabinet with continuous white noise (68 dB) in a Plexiglas chamber with a stainless-steel grid floor (Ugo Basil, Italy). Between each trial, the CFC chamber was cleaned with 70% ethanol. At the beginning of each trial the mice were allowed to explore the chamber for 120s, followed by a foot shock (0.7 mA, 2 s). After 30 s, mice were returned to their home-cage. During memory retrieval tests, mice were re-exposed to the context and allowed to explore for 2 min. Freezing behavior was analyzed by video tracking using

Ethovision XT (Noldus, the Netherlands) and was defined as a lack of movement for at least 1.5 s.

4-hydroxytamoxifen treatment

Mice received 4-hydroxytamoxifen (4TM, HB6040, HelloBio, 25 mg per kg, i.p.) 2 hours after CFC training. To make the 4TM aqueous solution, 15 mg 4TM was dissolved in 300 µl DMSO (D8418, Sigma-Aldrich Chemie N.V, The Netherlands). This solution was then further diluted with 2850 µl saline with 2% Tween80 (P1754, Sigma-Aldrich Chemie N.V, The Netherlands) saline and then with 2850 µl saline, making a solution of 2.5 mg 4TM per ml saline, 5% DMSO and 1% Tween80 (Matos et al., 2019; Ye et al., 2016).

Electrophysiological recordings

Mice were transcardially perfused with ice-cold partial sucrose solution (70 mM NaCl, 2.5 mM KCl, 1.25 $NaH_2PO_4*H_2O$, 5 mM $MgSO_4*7H_2O$, 1 mM $CaCl_2*2H_2O$, 70 mM sucrose, 25 mM D-glucose, 25 mM $NaHCO_3$, 1 mM sodium ascorbate and 3 mM sodium pyruvate, carboxygenated with 5% CO_2/95% O_2, pH 7.4, 310 mOsm), followed by decapitation and rapid extraction of the brain. 300 µm coronal slices were made from the mPFC in ice-cold carboxygenated partial sucrose solution using a vibratome (Leica). After 15 min of incubation at 37 °C in partial sucrose solution, slices were transferred to holding aCSF (125 mM NaCl, 3 mM KCl, 1.25 NaH_2PO_4*H2O, 2 mM $MgCl_2*6H_2O$, 1.3 mM $CaCl_2*2H_2O$, 25 mM D-glucose, 25 mM $NaHCO_3$, 1 mM sodium ascorbate and 3 mM sodium pyruvate, carboxygenated with 5% CO_2/95% O_2, pH 7.4, 310 mOsm). After a recovery step of 45 min at RT, slices were transferred to a recording chamber continuously perfused with carboxygenated running aCSF (holding aCSF without sodium ascorbate, sodium pyruvate and only 1 mM $MgCl_2*6H_2O$, 34 °C). The mPFC was identified using a differential interference contrast microscopy, and PV cells expressing tdTomato or SST cells expressing mCherry were found using fluorescence. Pyramidal, PV and SST cells were recorded in the mPFC using a Multiclamp 700B amplifier (Molecular devices, Sunnyvale, CA) and sampled at 10 kHz low pass filter at 4 kHz and digitized with Axon Digidata 1440 A (Molecular Devices). Whole cell recordings were done with borosilicate glass electrodes (Science Products, Hofheim, Germany) with tip resistance of 2-6 MOhm, filled with potassium-gluconate based intracellular (148 mM K-gluconate, 1 mM KCl, 10 mM HEPES, 0.3 mM EGTA, 4 mM K_2-phosphocreatinine, 4 mM Mg-ATP, 0.4 mM GTP, adjusted to pH 7.3-7.4 with KOH, 300 mOsm). Once a giga ohm seal was acquired, a whole cell configuration was obtained, and the resting membrane potential was directly recorded. Passive and active membrane properties of PV, SST and pyramidal neurons were measured in current clamp mode while being kept at -70 mV. Rheobase was analyzed using an incremental ramp like injection of current from 0 pA to ±400 pA for 1200 ms. An input-output profile was generated by injecting incrementally increasing currents, starting at -100 pA to 250 pA in steps of 25 pA for pyramidal and SST cells, and up to 425 pA for PV cells. Cells with an access resistance of above 25 mOhm as well as cells that showed unstable resting membrane potential or aberrant spiking patterns were excluded from analysis. Data was analyzed using a custom-made script in MATLAB (Mathworks). PYR cell recordings at 20 weeks were acquired from APP Parv Cre tdTomato and APP SST-Cre mice and control Parv Cre tdTomato and SST-Cre, respectively.

Animals used for sEPSC and sIPSC recordings were immediately sacrificed after remote memory retrieval similarly as described above. sEPSC and sIPSC recordings were

recorded using a cesium gluconate based intracellular (120 mM, 10 mM CsCl, 10 mM Hepes, 10 mM K-phosphocreatine, 2 ATP-Mg, 0.3 mM GTP, 0.2 mM EGTA and 1 mM QX314, adjusted to pH 7.3-7.4 with CsOH). sEPSCs were recorded at a holding potential of -70 mV and sIPSCs were recorded at 0 mV. Pyramidal cells expressing mCherry were identified using fluorescence, and pyramidal cells not expressing mCherry were recorded in the same field of view and identified based on morphology. Access resistance was monitored during recording and cells with an access resistance of above 20 mOhm were excluded. Cells with an unstable signal were excluded from analysis. Events were analyzed using TaroTools add on in IgorPro8.0 (Wavemetrics), where analysis was performed on 2 min of sEPSC and 1 min of sIPSC recordings.

Immunohistochemistry

Mice were transcardially perfused with ice-cold PBS (pH 7.4), followed by perfusion with ice-cold 4% paraformaldehyde (PFA) in PBS (pH 7.4). After removing the brains and overnight post-fixation in 4% PFA solution, the brains were immersed in 30% sucrose PBS solution with 0.02% NaN_3. Coronal sections of 35 µm were made using a cryostat and were stored at 4 °C in PBS with 0.02 NaN_3 until further use. Immunohistochemical staining were performed on free-floating brain sections as previously described (Van den Oever et al., 2013). The following antibodies were used: rabbit anti-fos (1:1000, 226008, SySy), mouse anti-parvalbumin (1:2000, MAB1572, Chemicon/Millipore), goat anti-rabbit Alexa Fluor 488 (1:400, A11008, ThermoFisher Scientific, USA), goat anti-mouse Alexa Fluor 405 (1:400, A31553, Invitrogen) and NeuroTrace™ 530/615 Red fluorescent Nissl (1:200, N21483, ThermoFisher Scientific, USA). First, sections were washed with PBS and blocked for one hour at room temperature with 0.2% Triton X-100 and 5% fetal bovine serum in PBS. Primary antibodies were diluted in blocking solution, which was used to incubate sections overnight at 4 °C. After primary antibody incubation, the sections were washed with PBS, followed by a 2-hour incubation step with the secondary antibody solution containing NeuroTrace™ Nissl at room temperature. Finally, sections were rinsed with PBS, mounted and cover slipped. To quantify the immunostainings, images of the mPFC were acquired using a confocal microscope (Nikon, Eclipse Ti2), where 6-8 z-stacks were made per animal. The experimenter was blind to the genotype. Similar exposure time, gain settings and camera settings were used in each set of experiments. Quantification of Nissl cells was done using ImageJ software, where regions of interest (ROIs) of cells where extracted. MATLAB (Mathworks) was used to correct for cells included in multiple ROIs in sequential z-stacks. Cells positive for mCherry, Fos or parvalbumin, and overlap thereof were counted manually using the ImageJ cell counter. To quantify PV labeling around $mCherry^+$ and $mCherry^-$ cells, we used a custom-made script in ImageJ to extract cell ROIs. The ROI was enlarged and used to measure the total amount of binarized PV labeling within the ring surrounding the cell. The total amount was normalized to the surface area of the ring. Using a custom-made script in MATLAB, data was categorized into $mCherry^+$ and neighboring $mCherry^-$ expressing neurons.

Statistical analyses

Statistical details are presented in the figure legends, where the number of animals and the number of cells is shown. Statistical testing was done using GraphPad Prism (version 10.4.1, San Diego, CA, USA). When comparing two groups, a paired Student's t-test were used for groups with normally distributed data and a Mann-Whitney U test was used for groups with

non-parametric data. For the comparisons of multiple groups, a repeated measure two-way ANOVA were used with a Bonferroni's test for post-hoc analysis. P-values <0.05 were considered significant. Statistical outliers were identified using Grubbs' test. Data is shown as mean ± standard error of the mean (SEM). Experimenters were blind to the genotype of the mice to reduce bias when analyzing data.

Acknowledgment

We thank Yvonne Gouwenberg for AAV packaging, Robbert Zalm for generating AAV constructs and Tim Heijstek for technical assistance in electrophysiology. We also thank Nine Kok and Romina Ambrosini for assistance with immunohistochemical stainings. Ronald van Kesteren and Michel van den Oever received funding from the Dutch Alzheimer Association (Alzheimer Nederland; grant: WE.03-2020-05).

References

Avgerinos, K. I., Manolopoulos, A., Ferrucci, L., & Kapogiannis, D. (2024). Critical assessment of anti-amyloid-β monoclonal antibodies effects in Alzheimer's disease: a systematic review and meta-analysis highlighting target engagement and clinical meaningfulness. *Scientific Reports*, *14*(1), 25741. https://doi.org/10.1038/s41598-024-75204-8

Buzsáki, G. (2002). Theta oscillations in the hippocampus. *Neuron*, *33*(3), 325-340. https://doi.org/10.1016/s0896-6273(02)00586-x

Buzsáki, G. (2010). Neural syntax: cell assemblies, synapsembles, and readers. *Neuron*, *68*(3), 362-385. https://doi.org/10.1016/j.neuron.2010.09.023

Celone, K. A., Calhoun, V. D., Dickerson, B. C., Atri, A., Chua, E. F., Miller, S. L., DePeau, K., Rentz, D. M., Selkoe, D. J., Blacker, D., Albert, M. S., & Sperling, R. A. (2006). Alterations in memory networks in mild cognitive impairment and Alzheimer's disease: an independent component analysis. *J Neurosci*, *26*(40), 10222-10231. https://doi.org/10.1523/jneurosci.2250-06.2006

Courtin, J., Chaudun, F., Rozeske, R. R., Karalis, N., Gonzalez-Campo, C., Wurtz, H., Abdi, A., Baufreton, J., Bienvenu, T. C. M., & Herry, C. (2014). Prefrontal parvalbumin interneurons shape neuronal activity to drive fear expression. *Nature*, *505*(7481), 92-96. https://doi.org/10.1038/nature12755

Cruz, F. C., Koya, E., Guez-Barber, D. H., Bossert, J. M., Lupica, C. R., Shaham, Y., & Hope, B. T. (2013). New technologies for examining the role of neuronal ensembles in drug addiction and fear. *Nature Reviews Neuroscience*, *14*(11), 743-754. https://doi.org/10.1038/nrn3597

Cummings, K. A., Bayshtok, S., Dong, T. N., Kenny, P. J., & Clem, R. L. (2022). Control of fear by discrete prefrontal GABAergic populations encoding valence-specific information. *Neuron*, *110*(18), 3036-3052.e3035. https://doi.org/10.1016/j.neuron.2022.07.004

Cummings, K. A., & Clem, R. L. (2020). Prefrontal somatostatin interneurons encode fear memory. *Nat Neurosci*, *23*(1), 61-74. https://doi.org/10.1038/s41593-019-0552-7

Dickerson, B. C., Salat, D. H., Greve, D. N., Chua, E. F., Rand-Giovannetti, E., Rentz, D. M., Bertram, L., Mullin, K., Tanzi, R. E., Blacker, D., Albert, M. S., & Sperling, R. A. (2005). Increased hippocampal activation in mild cognitive impairment compared to normal aging and AD. *Neurology*, *65*(3), 404-411. https://doi.org/10.1212/01.wnl.0000171450.97464.49

Donato, F., Rompani, S. B., & Caroni, P. (2013). Parvalbumin-expressing basket-cell network plasticity induced by experience regulates adult learning. *Nature*, *504*(7479), 272-276. https://doi.org/10.1038/nature12866

El Haj, M., Antoine, P., Nandrino, J. L., & Kapogiannis, D. (2015). Autobiographical memory decline in Alzheimer's disease, a theoretical and clinical overview. *Ageing Res Rev*, *23*(Pt B), 183-192. https://doi.org/10.1016/j.arr.2015.07.001

Fenno, L. E., Mattis, J., Ramakrishnan, C., Hyun, M., Lee, S. Y., He, M., Tucciarone, J., Selimbeyoglu, A., Berndt, A., Grosenick, L., Zalocusky, K. A., Bernstein, H., Swanson, H., Perry, C., Diester, I., Boyce, F. M., Bass, C. E., Neve, R., Huang, Z. J., & Deisseroth, K. (2014). Targeting cells with single vectors using multiple-feature Boolean logic. *Nat Methods*, *11*(7), 763-772. https://doi.org/10.1038/nmeth.2996

Filippini, N., MacIntosh, B. J., Hough, M. G., Goodwin, G. M., Frisoni, G. B., Smith, S. M., Matthews, P. M., Beckmann, C. F., & Mackay, C. E. (2009). Distinct patterns of brain

activity in young carriers of the APOE-epsilon4 allele. *Proc Natl Acad Sci U S A*, *106*(17), 7209-7214. https://doi.org/10.1073/pnas.0811879106

Frankland, P. W., & Bontempi, B. (2005). The organization of recent and remote memories. *Nat Rev Neurosci*, *6*(2), 119-130. https://doi.org/10.1038/nrn1607

Guenthner, C. J., Miyamichi, K., Yang, H. H., Heller, H. C., & Luo, L. (2013). Permanent genetic access to transiently active neurons via TRAP: targeted recombination in active populations. *Neuron*, *78*(5), 773-784. https://doi.org/10.1016/j.neuron.2013.03.025

Hijazi, S., Heistek, T. S., Scheltens, P., Neumann, U., Shimshek, D. R., Mansvelder, H. D., Smit, A. B., & van Kesteren, R. E. (2020). Early restoration of parvalbumin interneuron activity prevents memory loss and network hyperexcitability in a mouse model of Alzheimer's disease. *Mol Psychiatry*, *25*(12), 3380-3398. https://doi.org/10.1038/s41380-019-0483-4

Jackson, H. M., Soto, I., Graham, L. C., Carter, G. W., & Howell, G. R. (2013). Clustering of transcriptional profiles identifies changes to insulin signaling as an early event in a mouse model of Alzheimer's disease. *BMC Genomics*, *14*, 831. https://doi.org/10.1186/1471-2164-14-831

Jankowsky, J. L., Fadale, D. J., Anderson, J., Xu, G. M., Gonzales, V., Jenkins, N. A., Copeland, N. G., Lee, M. K., Younkin, L. H., Wagner, S. L., Younkin, S. G., & Borchelt, D. R. (2004). Mutant presenilins specifically elevate the levels of the 42 residue beta-amyloid peptide in vivo: evidence for augmentation of a 42-specific gamma secretase. *Hum Mol Genet*, *13*(2), 159-170. https://doi.org/10.1093/hmg/ddh019

Jankowsky, J. L., Slunt, H. H., Ratovitski, T., Jenkins, N. A., Copeland, N. G., & Borchelt, D. R. (2001). Co-expression of multiple transgenes in mouse CNS: a comparison of strategies. *Biomol Eng*, *17*(6), 157-165. https://doi.org/10.1016/s1389-0344(01)00067-3

Jankowsky, J. L., Xu, G., Fromholt, D., Gonzales, V., & Borchelt, D. R. (2003). Environmental enrichment exacerbates amyloid plaque formation in a transgenic mouse model of Alzheimer disease. *J Neuropathol Exp Neurol*, *62*(12), 1220-1227. https://doi.org/10.1093/jnen/62.12.1220

Josselyn, S. A., Köhler, S., & Frankland, P. W. (2015). Finding the engram. *Nat Rev Neurosci*, *16*(9), 521-534. https://doi.org/10.1038/nrn4000

Josselyn, S. A., & Tonegawa, S. (2020). Memory engrams: Recalling the past and imagining the future. *Science*, *367*(6473). https://doi.org/10.1126/science.aaw4325

Kimura, R., & Ohno, M. (2009). Impairments in remote memory stabilization precede hippocampal synaptic and cognitive failures in 5XFAD Alzheimer mouse model. *Neurobiol Dis*, *33*(2), 229-235. https://doi.org/10.1016/j.nbd.2008.10.006

Kitamura, T., Ogawa, S. K., Roy, D. S., Okuyama, T., Morrissey, M. D., Smith, L. M., Redondo, R. L., & Tonegawa, S. (2017). Engrams and circuits crucial for systems consolidation of a memory. *Science*, *356*(6333), 73-78. https://doi.org/10.1126/science.aam6808

Knopman, D. S., Amieva, H., Petersen, R. C., Chételat, G., Holtzman, D. M., Hyman, B. T., Nixon, R. A., & Jones, D. T. (2021). Alzheimer disease. *Nat Rev Dis Primers*, *7*(1), 33. https://doi.org/10.1038/s41572-021-00269-y

Lee, A. T., Vogt, D., Rubenstein, J. L., & Sohal, V. S. (2014). A class of GABAergic neurons in the prefrontal cortex sends long-range projections to the nucleus accumbens and elicits acute avoidance behavior. *J Neurosci*, *34*(35), 11519-11525. https://doi.org/10.1523/JNEUROSCI.1157-14.2014

Li, J., Wu, X., Tan, X., Wang, S., Qu, R., Wu, X., Chen, Z., Wang, Z., & Chen, G. (2023). The efficacy and safety of anti-Aβ agents for delaying cognitive decline in Alzheimer's disease: a meta-analysis [Systematic Review]. *Frontiers in Aging Neuroscience*, *15*. https://doi.org/10.3389/fnagi.2023.1257973

Liu, L., Liu, Y., Li, N., Huang, R., Zheng, X., Huang, L., Hou, S., & Yuan, Q. (2020). Multiple inflammatory profiles of microglia and altered neuroimages in APP/PS1 transgenic AD mice. *Brain Research Bulletin*, *156*, 86-104. https://doi.org/https://doi.org/10.1016/j.brainresbull.2020.01.003

Liu, X., Ramirez, S., Pang, P. T., Puryear, C. B., Govindarajan, A., Deisseroth, K., & Tonegawa, S. (2012). Optogenetic stimulation of a hippocampal engram activates fear memory recall. *Nature*, *484*(7394), 381-385. https://doi.org/10.1038/nature11028

Matos, M. R., Visser, E., Kramvis, I., van der Loo, R. J., Gebuis, T., Zalm, R., Rao-Ruiz, P., Mansvelder, H. D., Smit, A. B., & van den Oever, M. C. (2019). Memory strength gates the involvement of a CREB-dependent cortical fear engram in remote memory. *Nat Commun*, *10*(1), 2315. https://doi.org/10.1038/s41467-019-10266-1

Moore, T. L., Medalla, M., Ibañez, S., Wimmer, K., Mojica, C. A., Killiany, R. J., Moss, M. B., Luebke, J. I., & Rosene, D. L. (2023). Neuronal properties of pyramidal cells in lateral prefrontal cortex of the aging rhesus monkey brain are associated with performance deficits on spatial working memory but not executive function. *Geroscience*, *45*(3), 1317-1342. https://doi.org/10.1007/s11357-023-00798-2

Morrison, D. J., Rashid, A. J., Yiu, A. P., Yan, C., Frankland, P. W., & Josselyn, S. A. (2016). Parvalbumin interneurons constrain the size of the lateral amygdala engram. *Neurobiol Learn Mem*. https://doi.org/10.1016/j.nlm.2016.07.007

Palop, J. J., Chin, J., Roberson, E. D., Wang, J., Thwin, M. T., Bien-Ly, N., Yoo, J., Ho, K. O., Yu, G. Q., Kreitzer, A., Finkbeiner, S., Noebels, J. L., & Mucke, L. (2007). Aberrant excitatory neuronal activity and compensatory remodeling of inhibitory hippocampal circuits in mouse models of Alzheimer's disease. *Neuron*, *55*(5), 697-711. https://doi.org/10.1016/j.neuron.2007.07.025

Park, K., Kohl, M. M., & Kwag, J. (2024). Memory encoding and retrieval by retrosplenial parvalbumin interneurons are impaired in Alzheimer's disease model mice. *Current Biology*, *34*(2), 434-443.e434. https://doi.org/https://doi.org/10.1016/j.cub.2023.12.014

Perusini, J. N., Cajigas, S. A., Cohensedgh, O., Lim, S. C., Pavlova, I. P., Donaldson, Z. R., & Denny, C. A. (2017). Optogenetic stimulation of dentate gyrus engrams restores memory in Alzheimer's disease mice. *Hippocampus*, *27*(10), 1110-1122. https://doi.org/10.1002/hipo.22756

Popescu, I. R., Le, K. Q., Ducote, A. L., Li, J. E., Leland, A. E., & Mostany, R. (2021). Increased intrinsic excitability and decreased synaptic inhibition in aged somatosensory cortex pyramidal neurons. *Neurobiol Aging*, *98*, 88-98. https://doi.org/10.1016/j.neurobiolaging.2020.10.007

Roy, D. S., Arons, A., Mitchell, T. I., Pignatelli, M., Ryan, T. J., & Tonegawa, S. (2016). Memory retrieval by activating engram cells in mouse models of early Alzheimer's disease. *Nature*, *531*(7595), 508-512. https://doi.org/10.1038/nature17172

Schmid, L. C., Mittag, M., Poll, S., Steffen, J., Wagner, J., Geis, H. R., Schwarz, I., Schmidt, B., Schwarz, M. K., Remy, S., & Fuhrmann, M. (2016). Dysfunction of Somatostatin-Positive Interneurons Associated with Memory Deficits in an Alzheimer's Disease Model. *Neuron*, *92*(1), 114-125. https://doi.org/10.1016/j.neuron.2016.08.034

Somogyi, P., Freund, T. F., & Cowey, A. (1982). The axo-axonic interneuron in the cerebral cortex of the rat, cat and monkey. *Neuroscience*, *7*(11), 2577-2607. https://doi.org/https://doi.org/10.1016/0306-4522(82)90086-0

Stefanelli, T., Bertollini, C., Lüscher, C., Muller, D., & Mendez, P. (2016). Hippocampal Somatostatin Interneurons Control the Size of Neuronal Memory Ensembles. *Neuron*, *89*(5), 1074-1085. https://doi.org/10.1016/j.neuron.2016.01.024

Szegedi, V., Tiszlavicz, Á., Furdan, S., Douida, A., Bakos, E., Barzo, P., Tamas, G., Szucs, A., & Lamsa, K. (2024). Aging-associated weakening of the action potential in fast-spiking interneurons in the human neocortex. *J Biotechnol*, *389*, 1-12. https://doi.org/10.1016/j.jbiotec.2024.04.020

Tremblay, R., Lee, S., & Rudy, B. (2016). GABAergic Interneurons in the Neocortex: From Cellular Properties to Circuits. *Neuron*, *91*(2), 260-292. https://doi.org/10.1016/j.neuron.2016.06.033

Trouche, S., Sasaki, J. M., Tu, T., & Reijmers, L. G. (2013). Fear extinction causes target-specific remodeling of perisomatic inhibitory synapses. *Neuron*, *80*(4), 1054-1065. https://doi.org/10.1016/j.neuron.2013.07.047

Van den Oever, M. C., Rotaru, D. C., Heinsbroek, J. A., Gouwenberg, Y., Deisseroth, K., Stuber, G. D., Mansvelder, H. D., & Smit, A. B. (2013). Ventromedial prefrontal cortex pyramidal cells have a temporal dynamic role in recall and extinction of cocaine-associated memory. *J Neurosci*, *33*(46), 18225-18233. https://doi.org/10.1523/jneurosci.2412-13.2013

Végh, M. J., Heldring, C. M., Kamphuis, W., Hijazi, S., Timmerman, A. J., Li, K. W., van Nierop, P., Mansvelder, H. D., Hol, E. M., Smit, A. B., & van Kesteren, R. E. (2014). Reducing hippocampal extracellular matrix reverses early memory deficits in a mouse model of Alzheimer's disease. *Acta Neuropathol Commun*, *2*, 76. https://doi.org/10.1186/s40478-014-0076-z

Veres, J. M., Nagy, G. A., Vereczki, V. K., Andrási, T., & Hájos, N. (2014). Strategically Positioned Inhibitory Synapses of Axo-axonic Cells Potently Control Principal Neuron Spiking in the Basolateral Amygdala. *The Journal of Neuroscience*, *34*(49), 16194. https://doi.org/10.1523/JNEUROSCI.2232-14.2014

Wolff, S. B., Gründemann, J., Tovote, P., Krabbe, S., Jacobson, G. A., Müller, C., Herry, C., Ehrlich, I., Friedrich, R. W., Letzkus, J. J., & Lüthi, A. (2014). Amygdala interneuron subtypes control fear learning through disinhibition. *Nature*, *509*(7501), 453-458. https://doi.org/10.1038/nature13258

Ye, L., Allen, W. E., Thompson, K. R., Tian, Q., Hsueh, B., Ramakrishnan, C., Wang, A. C., Jennings, J. H., Adhikari, A., Halpern, C. H., Witten, I. B., Barth, A. L., Luo, L., McNab, J. A., & Deisseroth, K. (2016). Wiring and Molecular Features of Prefrontal Ensembles Representing Distinct Experiences. *Cell*, *165*(7), 1776-1788. https://doi.org/10.1016/j.cell.2016.05.010

Yiu, A. P., Mercaldo, V., Yan, C., Richards, B., Rashid, A. J., Hsiang, H. L., Pressey, J., Mahadevan, V., Tran, M. M., Kushner, S. A., Woodin, M. A., Frankland, P. W., & Josselyn, S. A. (2014). Neurons are recruited to a memory trace based on relative neuronal excitability immediately before training. *Neuron*, *83*(3), 722-735. https://doi.org/10.1016/j.neuron.2014.07.017

Zhou, Y., Qiu, L., Wang, H., & Chen, X. (2020). Induction of activity synchronization among primed hippocampal neurons out of random dynamics is key for trace memory

formation and retrieval. *Faseb j*, *34*(3), 3658-3676. https://doi.org/10.1096/fj.201902274R

Zhou, Y., Won, J., Karlsson, M. G., Zhou, M., Rogerson, T., Balaji, J., Neve, R., Poirazi, P., & Silva, A. J. (2009). CREB regulates excitability and the allocation of memory to subsets of neurons in the amygdala. *Nat Neurosci*, *12*(11), 1438-1443. http://www.ncbi.nlm.nih.gov/entrez/query.fcgi?cmd=Retrieve&db=PubMed&dopt=Citation&list_uids=19783993

Supplemental figures

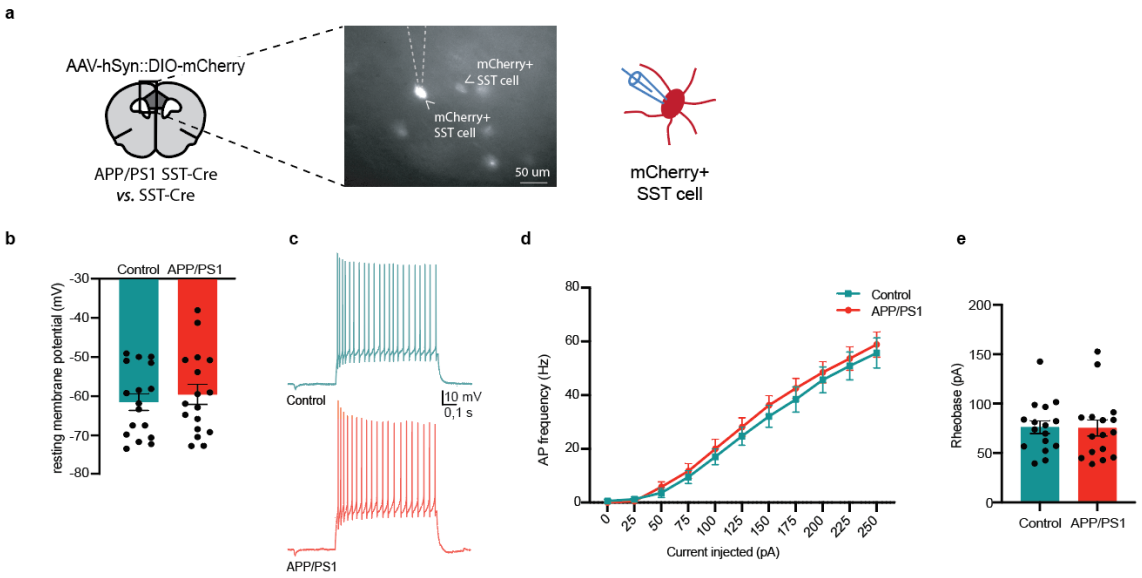

Sup. Fig. 1: SST cell excitability is unaltered in the mPFC of 20-week-old APP/PS1 mice. **a.** Schematic coronal brain section indicating the mPFC prelimbic region in dark grey, where AAV-hSyn::DIO-mCherry was microinjected and mCherry^{+} SST cells were recorded in APP/PS1 SST-Cre (APP/PS1) and SST-Cre (control) mice. Representative fluorescent image is depicted **b.** Resting membrane potential was unaltered in SST cells. Unpaired t-test: t_{31} = 0.73, p = 0.47, n = 17/16 cells, N = 5/7 control vs. APP/PS1 mice, respectively. **c.** Action potential (AP) firing of SST cells upon a depolarizing current step (250 pA) **d.** AP frequency in SST cells in response to 0-250 pA depolarizing current steps did not differ between genotypes. *Genotype x current* two-way repeated measures ANOVA $F_{(10,310)}$ = 0.23, p = 0.99, n = 17/16 cells, N = 5/7 control vs. APP/PS1 mice. **e.** Rheobase was unchanged in SST cells Mann-Whitney test: U = 119, p = 0.75, n = 17/16 cells, N = 5/7 control vs. APP/PS1 mice, respectively. Graphs show mean ± s.e.m.

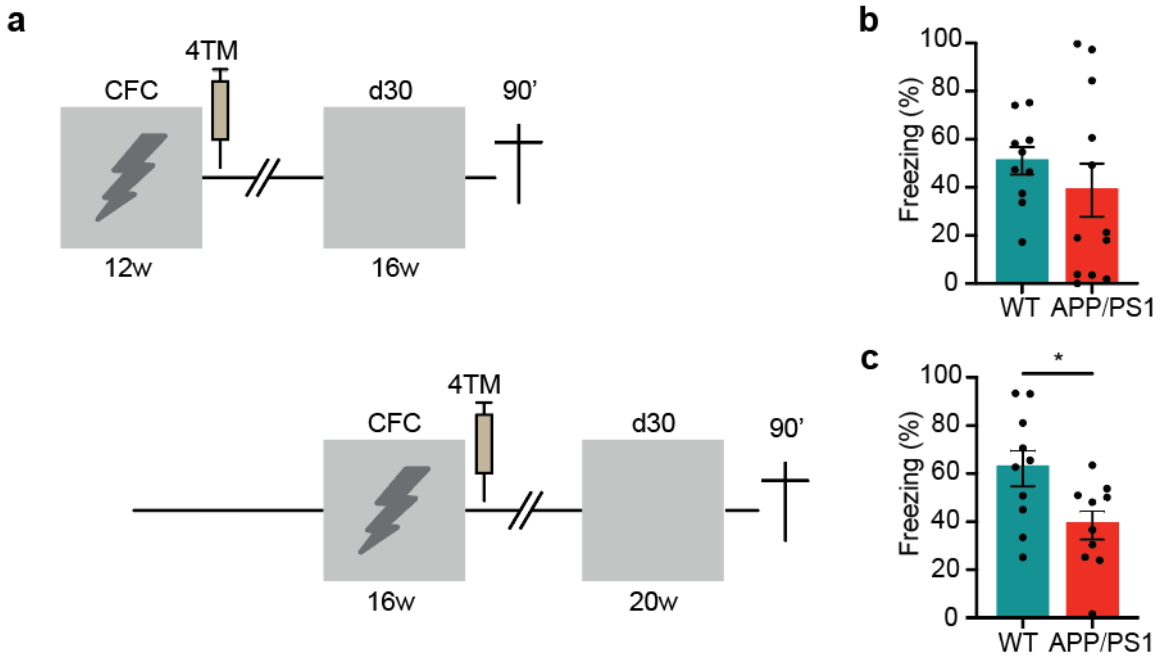

Sup. Fig. 2. APP/PS1 mice show remote memory impairment at 20, but not 16, weeks of age **a.** Experimental design. WT and APP/PS1 mice underwent CFC at 12 and 16 weeks of age, and memory retrieval 30 days later. Mice received an injection of 4-hydroxy tamoxifen (4TM) 2 hours after CFC to tag mPFC engram cells. **b.** At 16 weeks old, APP/PS1 mice did not differ in freezing levels compared to WT controls. Mann Whitney test: $U = 46$, $p = 0.38$, WT ($n = 10$), APP/PS1 ($n = 12$). **c.** At 20 weeks old, APP/PS1 mice show reduced freezing levels compared to WT controls. Unpaired t-test: $t_{18} = 2.50$, $*p = 0.022$, WT ($n = 10$), APP/PS1 ($n = 10$). Graphs show mean ± s.e.m.

Supplemental tables

Supplementary Table 1. Passive and active membrane properties of PV interneurons in the mPFC at 16 weeks			
	PV interneurons		
Properties	**PV-Cre-tdTomato** (mean ± SEM)	**APP/PS1-PV-Cre-tdTomato** (mean ± SEM)	***p-value*** (Student's *t*-test)
Passive properties			
RMP (mV)	-71.6 ± 0.88	-71.1±1.04	*0.98*
Rheobase (pA)	258.1±16.60	256.3±14.57	*0.93*
Current threshold (mV)	-30.7±1.17	-32.1±0.71	*0.3*
Input resistance (Mohm)	94.2±3.48	93.4±5.44	*0.50*
Membrane capacitance (pF)	129.7±9.23	99.7±4.45	**0.010*
Sag ratio	0.062±0.007	0.063±0.004	*0.90*
Time constant (ms)	5.74±0.39	5.46±0.25	*0.55*
Active properties			
AP amplitude (mV)	53.4±1.19	51.9±0.98	*0.34*
AP half-width (msec)	0.38±0.012	0.40±0.010	*0.38*
AHP (mV)	-18.3±0.48	-17.6±0.45	*0.32*
AHP time to peak (ms)	1.28±0.070	1.31±0.045	*0.24*
dv/dtmin (mV/ms)	-182.1±8.14	-167.6±5.57	*0.15*
dv/dtmax (mV/ms)	284.5±9.61	265.80±6.33	*0.11*
Interspike interval (ms)	16.4±0.71	17.0±0.83	*0.61*
Adaptation ratio	1.02±0.031	1.09±0.063	*0.72*

Supplementary Table 2. Passive and active membrane properties of PYR neurons in the mPFC at 16 weeks

	PYR neurons		
Properties	**PV-Cre-tdTomato** (mean ± SEM)	**APP/PS1-PV-Cre-tdTomato** (mean ± SEM)	***p-value*** (Student's *t*-test)
Passive properties			
RMP (mV)	-65.3 ± 1.46	-64.1±1.87	*0.61*
Rheobase (pA)	161.7±19.39	110.5±13.66	**0.048*
Current threshold (mV)	-39.5±1.27	-42.1±0.84	*0.09*
Input resistance (Mohm)	124.4±13.93	141.7±9.54	*0.30*
Membrane capacitance (pF)	158.5±9.04	149.8±8.23	*0.48*
Sag ratio	0.12±0.017	0.12 ±0.012	*0.89*
Time constant (ms)	21.7±1.86	26.8±2.32	*0.10*
Active properties			
AP amplitude (mV)	84.8±4.23	79.1±2.09	*0.52*
AP half-width (msec)	1.26±0.096	1.50±0.054	**0.002*
AHP (mV)	-13.5±0.78	-13.2±0.86	*0.81*
AHP time to peak (ms)	42.6±3.55	45.1±3.47	*0.62*
dv/dtmin (mV/ms)	-58.3±5.18	-49.1±2.55	*0.12*
dv/dtmax (mV/ms)	258.9±24.10	215.9±12.05	*0.10*
Interspike interval (ms)	47.6±2.44	52.3±2.03	*0.14*
Adaptation ratio	0.39±0.046	0.49±0.032	*0.07*

865
866

Supplementary Table 3. Passive and active membrane properties of PV interneurons in the mPFC at 20 weeks

	PV interneurons		
Properties	**PV-Cre-tdTomato** (mean ± SEM)	**APP/PS1-PV-Cre-tdTomato** (mean ± SEM)	***p-value*** (Student's *t*-test)
Passive properties			
RMP (mV)	-70.22±0.65	-71.2±0.75	*0.36*
Rheobase (pA)	307.4±16.18	265.4±19.17	*0.10*
Current threshold (mV)	-34.7±0.70	-36.6±1.24	*0.17*
Input resistance (Mohm)	83.7±3.16	89.6±4.49	*0.28*
Membrane capacitance (pF)	64.8±3.36	68.1±5.67	*0.61*
Sag ratio	0.10±0.0051	0.10±0.0057	*0.57*
Time constant (ms)	6.1±0.27	6.2±0.32	*0.63*
Active properties			
AP amplitude (mV)	59.1±1.42	59.1±1.43	*0.99*
AP half-width (msec)	0.46±0.011	0.46±0.014	*0.71*
AHP (mV)	-19.2±0.37	-18.6±0.43	*0.31*
AHP time to peak (ms)	1.37±0.047	1.39±0.056	*0.76*
dv/dtmin (mV/ms)	-158.9±7.45	-157.1±8.32	*0.87*
dv/dtmax (mV/ms)	243.7±8.35	239.8±9.04	*0.76*
Interspike interval (ms)	23.2±1.73	21.9±1.37	*0.61*
Adaptation ratio	1.30±0.318	1.04±0.050	*0.58*

867
868

Supplementary Table 4. Passive and active membrane properties of PYR neurons in the mPFC at 20 weeks

	PYR neurons		
Properties	**PV-Cre** (mean ± SEM)	**APP/PS1-PV-Cre** (mean ± SEM)	***p-value*** (Student's *t*-test)
Passive properties			
RMP (mV)	-67.3±0.95	-65.9±1.09	*0.36*
Rheobase (pA)	130.2±8.85	104.3±6.79	**0.022*
Current threshold (mV)	-40.4±0.54	-40.8±0.53	*0.64*
Input resistance (Mohm)	125.6±8.64	136.0±9.63	*0.48*
Membrane capacitance (pF)	163.3±9.11	167.0±9.19	*0.78*
Sag ratio	0.14±0.013	0.13±0.009	*0.94*
Time constant (ms)	23.2±1.40	24.8±1.10	*0.39*
Active properties			
AP amplitude (mV)	84.1±1.75	84.7±1.03	*0.79*
AP half-width (msec)	1.25±0.035	1.17±0.024	*0.16*
AHP (mV)	-13.0±0.47	-12.9±0.42	*0.84*
AHP time to peak (ms)	34.7±1.99	34.8±1.38	*0.98*
dv/dtmin (mV/ms)	-58.4±2.23	-63.1±1.66	*0.10*
dv/dtmax (mV/ms)	263.2±11.57	267.4±7.43	*0.76*
Interspike interval (ms)	69.7±1.20	69.0±1.10	*0.67*
Adaptation ratio	0.50±0.027	0.44±0.023	*0.09*

Supplementary Table 5. Passive and active membrane properties of SST interneurons in the mPFC at 20 weeks

	SST interneurons		
Properties	**PV-Cre** (mean ± SEM)	**APP/PS1-PV-Cre** (mean ± SEM)	***p-value*** (Student's *t*-test)
Passive properties			
RMP (mV)	-61.2±2.14	-58.7±1.22	*0.47*
Rheobase (pA)	76.2±6.50	75.4±8.20	*0.75*
Current threshold (mV)	-41.9±1.24	-42.2±1.09	*0.86*
Input resistance (Mohm)	200.2±15.03	202.0±11.74	*0.93*
Membrane capacitance (pF)	98.4±6.33	86.6±6.14	*0.20*
Sag ratio	0.16±0.012	0.16±0.018	*0.9*
Time constant (ms)	21.7±2.09	20.9±1.75	*0.77*
Active properties			
AP amplitude (mV)	72.3±2.16	69.5±1.90	*0.34*
AP half-width (msec)	0.74±0.04	0.75±0.06	*0.83*
AHP (mV)	-13.1±1.31	-14.3±1.54	*0.55*
AHP time to peak (ms)	2.1±0.15	2.1±0.23	*0.78*
dv/dtmin (mV/ms)	-113.8±9.41	-114.0±10.56	*0.99*
dv/dtmax (mV/ms)	204.5±13.56	187.3±13.01	*0.37*
Interspike interval (ms)	53.0±4.09	43.4±3.7	*0.18*
Adaptation ratio	0.57±0.04	0.61±0.04	*0.48*

871